Hindawi
Advances in Mathematical Physics
Volume 2023, Article ID 9951245, 12 pages
https://doi.org/10.1155/2023/9951245

Research Article

Analysis and Prediction of the Dynamic Antiplane Characteristics of an Elastic Wedge-Shaped Quarter-Space Containing a Circular Hole

Shen Liu, Jie Yang, Yue Liu, and Qin Liu

School of Mechanical Engineering, Shanghai Dianji University, Shanghai 201306, China

Correspondence should be addressed to Jie Yang; yangj@sdju.edu.cn

Received 17 December 2022; Revised 9 March 2023; Accepted 18 March 2023; Published 30 March 2023

Academic Editor: Ivan Giorgio

Based on the wave function expansion method, the dynamic antiplane characteristics of a wedge-shaped quarter-space containing a circular hole are studied in a complex coordinate system. The wedge-shaped medium is decomposed into two subregions along the virtual boundary using the virtual region decomposition method. The scattering wave field in subregion I is constructed by the mirror method, and the standing wave field in region II is constructed by the fractional Bessel function. According to the continuity conditions at the virtual boundary and the stress-free boundary of the circular hole, the unknown coefficients of the wave fields are obtained by the Fourier integral transform, and the analytical solution of the dynamic stress concentration factor (DSCF) of the circular hole is then obtained. Through parametric analysis, the effects of incident wave frequency, geometry of the wedge, and corner slope on the DSCF of the circular hole are discussed. The results show that when the SH-wave is horizontally incidence at high frequencies, the DSCF of the circular hole can be significantly changed by introducing the corner slope. Moreover, when the corner slope is high, the maximum DSCF can be amplified about 1.2 times. Finally, the back propagation (BP) neural network prediction model of DSCF is established, and the coefficient of regression is found to reach more than 0.99.

1. Introduction

In the field of engineering, there are inevitably different types of defects in natural environments and engineering materials, of which circular defects are the most common. The presence of defects leads to the phenomenon of stress concentration, which may lead to the failure of the structure [1, 2]. Therefore, the stress concentration analysis of a certain structure has always been one of the important research topics in the field of nondestructive testing and fatigue life prediction.

Since a structure is prone to wear and fracture at the corner points during construction and use, the whole structure can be regarded as a wedge structure with a corner slope. The change in structure shape affects the stress concentration of the original structure and has a great influence on the durability of structure [3, 4]. In recent years, researchers have begun to pay attention to wedge-shaped mediums in engineering applications. Based on the wave function expansion method and weighted residual method, Lee et al. [5–7] studied the diffraction of an elastic wave by an arbitrary shape rigid body and depression in a wedge half-space, and then the scattering problem of the SH-wave in the wedge space was solved in polar coordinates with the virtual region decomposition method [8]. Shi et al. [9–12] used the wave function expansion method to obtain an analytical solution for the DSCF of the corner point defect and circular hole in the wedge space. Liu et al. [13] used the Green function method and the complex function method together with multipole coordinate transformation to analyze the dynamic antiplane characteristics of a circular hole in an infinite wedge space. Liang et al. [14, 15] considered the scattering of SH waves by a circular canyon and an alluvial valley in a wedge space and solved the problem using the great arc theorem and the Fourier series expansion method. Kara [16, 17] used the wave function expansion method and the

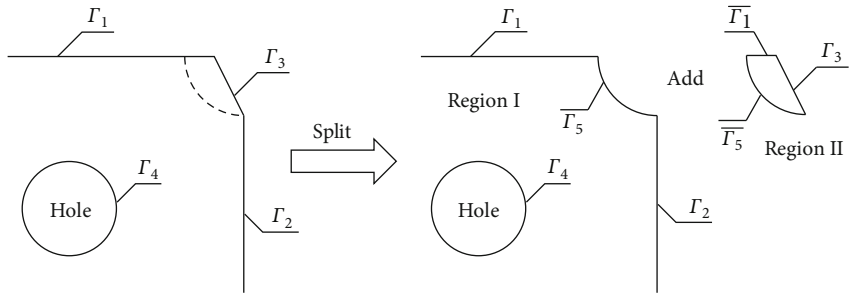

Figure 1: The virtual region decomposition model.

image method to solve the SH-wave scattering problem in a wedge space with a certain angle wedge space containing circular hole or tunnel. Based on the complex function method, Yang et al. [18, 19] studied the scattering of SH-wave by a circular canyon in a wedge space of inhomogeneous medium.

The above researches have mainly used semianalytical methods to study the antiplane characteristics of wedge spaces. In addition, there are some researches based on the boundary element method, the finite element method, and other numerical methods. Treifi et al. [20] used the finite element method to calculate the dynamic stress intensity factor (DSIF) at the tip of a wedge joint under reverse plane shear loading. Cheng et al. [21] analyzed the stress singularities near the tip of a wedge joint by the boundary element method and the characteristic expansion method. Ping et al. [22] analyzed the mechanical stress at the tip of a wedge combination based on a new finite element method. Based on the theory of single-layer potential and boundary element method, Liu et al. [23, 24] solved the scattering problem of the SH-wave by creating circular holes and linings in an elastic wedge space. Mieczkowski et al. [25] conducted finite element modeling of a wedge structure and analyzed the singular stress field at the sharp corner. In recent years, machine learning has been widely used in structural damage prediction and fatigue life prediction of materials [26]. There are also some studies on wedge structure-related issues. Sen et al. [27] used an artificial neural network to predict the load-bearing capacity of two circular holes in a wedge composite laminate. Based on the finite element method, Salman et al. [28] used artificial neural network to predict the geometric features of defects in wedge specimens.

It can be seen from the existing studies that most of the current problems are focused on the wedge space problem, and the wedge combination problem where the horizontal boundary and the inclined boundary are combined at arbitrary angles. There are few studies on the dynamic antiplane characteristics of a wedge-shaped quarter-space containing a circular hole. In this paper, the dynamic antiplane characteristics of a shallow circular hole embedded in a wedge-shape medium are investigated using the virtual region decomposition method in complex coordinates. The domain of the wedge model is divided into subregion I with a rounded corner and subregion II with a cut corner (see Figure 1 for details). The scattering wave field generated by the circular

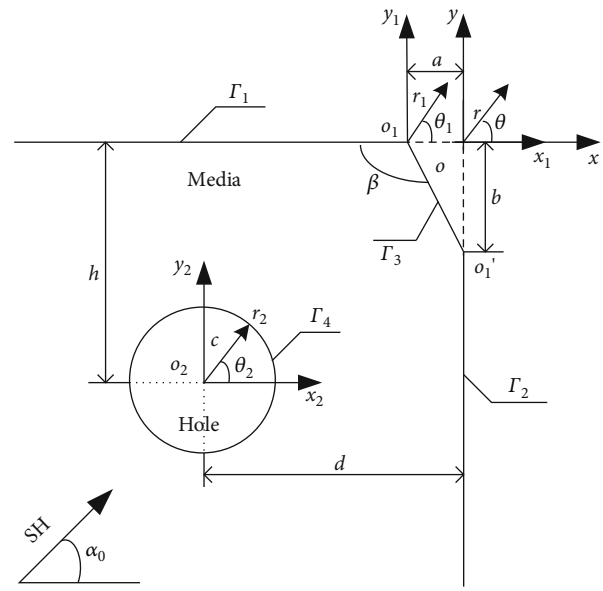

Figure 2: The theoretical model.

hole and the virtual boundary in subregion I are constructed by using the method of a mirror, and the standing wave field in subregion II is constructed by using the fractional Bessel function. By combining the boundary conditions and the continuity conditions, the integral equations of the definite solution are established and solved, and the analytical solution of the DSCF of the circular hole is obtained. A parametric analysis is then carried out to discuss the influence of different factors on DSCF. Finally, the BP neural network is used to build a prediction model for the dynamic antiplane characteristics of a circular hole embedded in an elastic wedge-shaped quarter-space. The predicted results are in good agreement with the expected results.

2. Theoretical Model and Boundary Conditions

The theoretical model of the problem is shown in Figure 2 where α_0 is the incident angle of the SH-wave, which is positive when it rotates counterclockwise in the positive direction of the x-axis. In addition, Γ_1, Γ_2, Γ_3, and Γ_4 are the horizontal boundary, vertical boundary, corner point slope boundary, and the circular hole boundary, respectively. Note that the angle between Γ_1 and Γ_3 is β. A global coordinate

system with origin at o (xoy), and two local coordinate systems with origins o_1 and o_2 ($x_1o_1y_1$ and $x_2o_2y_2$) are considered. Note that a and b are the distances from the origin of coordinate o to corner points o_1 and $o_1{}'$ (assuming $a < b$), and c is the radius of the circular hole. Moreover, h and d are the distances between the center of the circle and the boundary Γ_1 and Γ_2, respectively.

In the polar coordinate system, the displacement function $W(r,\theta)$ generated by the steady-state incident SH-wave satisfies the Helmholtz equation in the isotropic homogeneous continuous media, as follows

$$\frac{\partial^2 W}{\partial r^2} + \frac{1}{r}\frac{\partial W}{\partial r} + \frac{1}{r^2}\frac{\partial^2 W}{\partial \theta^2} + k^2 W = 0, \tag{1}$$

where k is the number of incident wave, its relationship with the frequency ω, and the speed of the shear wave c_s is $k = \omega/c_s$, while the relationship between c_s and media parameters is $c_s = \sqrt{\mu/\rho}$, where μ and ρ are the shear elastic modulus and the density of the media, respectively.

The harmonic relation between the displacement function and the time is $e^{-i\omega t}$. In Cartesian coordinates, Equation (1) can be expressed as

$$\frac{\partial^2 W}{\partial x^2} + \frac{\partial^2 W}{\partial y^2} + k^2 W = 0. \tag{2}$$

To facilitate the mutual conversion of the global coordinate system and the local coordinate system, complex coordinate system $(z, \bar{z})$ is introduced to Equation (2). Therefore, we have

$$\frac{\partial^2 W}{\partial z \partial \bar{z}} + \frac{1}{4}k^2 W = 0. \tag{3}$$

According to Hooke's law, the radial stress τ_{rz} and the circumferential stress $\tau_{\theta z}$ in the polar coordinate system are expressed as

$$\begin{aligned} \tau_{rz} &= \mu\left(\frac{\partial W}{\partial z}e^{i\theta} + \frac{\partial W}{\partial \bar{z}}e^{-i\theta}\right), \\ \tau_{\theta z} &= \boldsymbol{i}\mu\left(\frac{\partial W}{\partial z}e^{i\theta} - \frac{\partial W}{\partial \bar{z}}e^{-i\theta}\right), \end{aligned} \tag{4}$$

where $r = \sqrt{x^2 + y^2}$, $\theta = \arctan(y/x)$, $z = re^{i\theta}$, $\bar{z} = re^{-i\theta}$, i is imaginary number unit, and $i^2 = -1$.

In the theoretical model, the boundaries Γ_1, Γ_2, Γ_3, and Γ_4 satisfy the stress-free conditions

$$\Gamma_1 : \tau_{\theta z} = 0, (\theta = \pi), \tag{5}$$

$$\Gamma_2 : \tau_{\theta z} = 0, \left(\theta = \frac{3\pi}{2}\right), \tag{6}$$

$$\Gamma_3 : \tau_{\theta_1 z_1} = 0, (\theta_1 = \pi + \beta), \tag{7}$$

$$\Gamma_4 : \tau_{r_2 z_2} = 0, (0 \le \theta_2 \le 2\pi, r_2 = c), \tag{8}$$

where $\tau_{\theta z}$ is the circumferential stress at the boundaries Γ_1 and Γ_2; $\tau_{\theta_1 z_1}$ is the circumferential stress at the boundary Γ_3; and $\tau_{r_2 z_2}$ is the radial stress at the boundary Γ_4.

3. Virtual Region Decomposition and Wave Field Construction

3.1. Virtual Region Decomposition. Due to the existence of the specific boundary Γ_3, it is difficult to directly obtain the solutions to the wave field problem that satisfy the governing equation and boundary conditions in the whole domain. Therefore, the method of virtual region decomposition is used to obtain the wave field solutions with regular boundary subregions and then assembled to obtain the global solution. Virtual region decomposition is shown in Figure 1. When $a < b$, b is taken as the radius and o as the center of the circle to draw the arc for cutting (otherwise, a is taken as the radius). The whole region is decomposed into subregion I containing the circular hole and a subregion II containing a special boundary Γ_3 along the virtual boundary.

The boundary conditions at Γ_1 and Γ_2 should be satisfied when the wave field in subregion I is constructed. Similarly, the boundary conditions at $\overline{\Gamma_1}$ and Γ_3 should be satisfied when the wave field in subregion II is constructed. The continuity conditions of common boundaries Γ_5 and $\overline{\Gamma_5}$ are

$$W^{\mathrm{I}}(r,\theta) = W^{\mathrm{II}}(r,\theta) \quad (\pi \le \theta \le 3\pi/2, r = b), \tag{9}$$

$$\tau_{rz}^{\mathrm{I}}(r,\theta) = \tau_{rz}^{\mathrm{II}}(r,\theta) \quad (\pi \le \theta \le 3\pi/2, r = b), \tag{10}$$

where W^{I} and W^{II} are wave fields in region I and II, while τ_{rz}^{I} and τ_{rz}^{II} are radial stresses in region I and II.

3.2. Construction of the Free Wave Field. According to the available literature [29, 30], in the global coordinate system $(z, \bar{z})$, the equivalent incident wave field $W^{(i,e)}$ and the equivalent reflected wave field $W^{(r,e)}$ are expressed as

$$\begin{aligned} W^{(i,e)}(z,\bar{z}) &= W_0\left\{\left\{\exp\frac{\boldsymbol{i}k}{2}\left(ze^{-i\alpha_0} + \bar{z}e^{i\alpha_0}\right)\right\} + \left\{\exp\frac{\boldsymbol{i}k}{2}\left(ze^{-i\gamma_0} + \bar{z}e^{i\gamma_0}\right)\right\}\right\}, \\ W^{(r,e)}(z,\bar{z}) &= W_1\left\{\left\{\exp\frac{\boldsymbol{i}k}{2}\left(ze^{-i\alpha_1} + \bar{z}e^{i\alpha_1}\right)\right\} + \left\{\exp\frac{\boldsymbol{i}k}{2}\left(ze^{-i\gamma_1} + \bar{z}e^{i\gamma_1}\right)\right\}\right\}, \end{aligned} \tag{11}$$

where W_0 is the displacement amplitude of the incident wave, and W_1 is the displacement amplitude of the reflected wave. In this paper, we assumed that $W_1 = W_0$. In addition, $\gamma_0 = \pi - \alpha_0$ is the incident angle of the virtual point source in the global coordinate system, $\alpha_1 = -\alpha_0$ is the reflection angle, and $\gamma_1 = \pi - \alpha_1$.

3.3. Construction of the Scattered Wave Field. According to the available literature [9, 12, 31, 32], the scattered wave field

$W^{(s1)}$ at the corner point of the defect problem and the scattered wave field $W^{(s2)}$ in the half-space problem can be expressed as:

$$\begin{aligned} W^{(s1)}(r,\theta) &= \sum_{n=0}^{\infty} D_n H_{2n}^{(1)}(kr)\cos 2n\theta, \\ W^{(s2)}(r,\theta) &= \sum_{n=0}^{\infty} P_n H_{2n}^{(1)}(kr)\cos 2n\theta \\ &\quad + \sum_{n=0}^{\infty} Q_n H_{2n}^{(1)}(kr)\sin(2n+1)\theta, \end{aligned} \tag{12}$$

where D_n, P_n, Q_n are the undetermined coefficients and $H_n^{(1)}(\cdot)$ is the Hankel function of the first class of order n, $n = 0, 1, 2\cdots$.

Because of the existence of sine and cosine terms, these two forms often need to use Graf's addition theorem for coordinate transformation, and the solution is relatively complicated. Therefore, in this paper, the scattering wave field generated by the circular arc depression of the corner point and the circular hole in subregion I is constructed by the method of mirror. The mirror model is shown in Figure 3.

The scattered wave field $W^{(s3)}$ of the circular arc depression is different from the existing scattered wave field form of the corner point defects, and its expression is shown in Equation (13). This form of the scattered wave field satisfies the governing equation and the stress-free conditions at the boundary, and does not include sine and cosine terms. In the complex coordinate system, the mutual transformation between the global coordinate system and the local coordinate system can be easily done, and the problem-solving process is simplified.

$$\begin{aligned} W^{(s3)}(z,\bar{z}) = W_0 \sum_{-\infty}^{\infty} A_n \Bigg\{ & H_n{}^{(1)}(k|z|)\left(\frac{z}{|z|}\right)^n \\ & + H_n{}^{(1)}(k|z|)\left(\frac{z}{|z|}\right)^{-n} + (-1)^n H_n{}^{(1)}(k|z|) \\ & \cdot \left(\frac{z}{|z|}\right)^{-n} + (-1)^n H_n{}^{(1)}(k|z|)\left(\frac{z}{|z|}\right)^n \Bigg\}, \end{aligned} \tag{13}$$

where A_n is an unknown coefficient that can be determined by the continuity conditions of the circular arc at the depression boundary.

The scattered wave field $W^{(s4)}$ generated by the circular hole can be expressed as

$$\begin{aligned} W^{(s4)}(z_2,\overline{z_2}) = W_0 \sum_{n=-\infty}^{\infty} B_n \Big\{ & H_n^{(1)}(k|z_2|)[z_2/|z_2|]^n \\ & + H_n^{(1)}(k|z_3|)[z_3/|z_3|]^{-n} \\ & + (-1)^n H_n^{(1)}(k|z_4|)[z_4/|z_4|]^{-n} \\ & + (-1)^n H_n^{(1)}(k|z_5|)[z_5/|z_5|]^n \Big\}, \end{aligned} \tag{14}$$

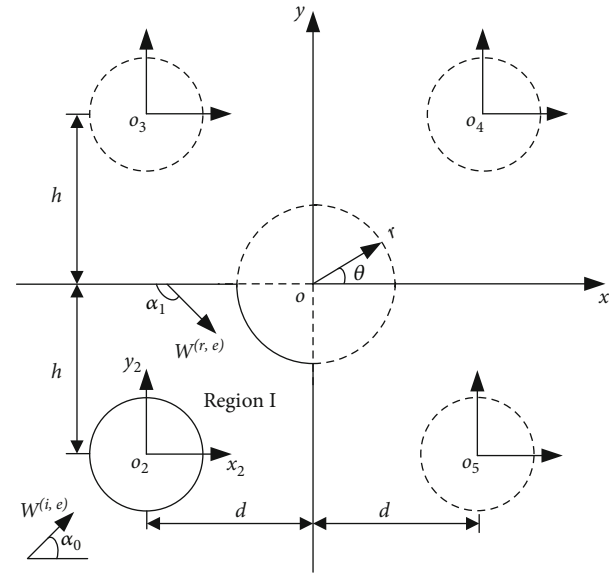

Figure 3: The mirror model.

where $z_2 = z + d + \mathrm{i}h$, $z_3 = z_2 - \boldsymbol{i}2h$, $z_4 = z_3 - 2d$, and $z_5 = z_2 - 2d$. In addition, B_n is an unknown coefficient that can be determined by applying stress-free boundary conditions of stress-free at the circular hole.

3.4. Construction of the Standing Wave Field. The standing wave field W^D satisfying the boundary conditions at $\overline{\Gamma_1}$ and Γ_3 in subregion II is constructed in the local coordinate system $(z_1, \overline{z_1})$ and can be expressed as

$$\begin{aligned} W^D(z_1,\overline{z_1}) = W_0 \sum_{n=-\infty}^{\infty} C_n \Bigg\{ & J_{np}(k|z_1|)\left(\frac{z_1}{|z_1|}\right)^{np} \\ & + J_{np}(k|z_1|)\left(\frac{z_1}{|z_1|}\right)^{-np} \Bigg\}, \end{aligned} \tag{15}$$

where $z_1 = z + a$, C_n is an unknown coefficient that can be determined by the boundary conditions, $J_{np}(\cdot)$ is the fractional Bessel function, and $p = \pi/\beta$ ($\pi/2 < \beta < \pi$).

4. Equation Solving and Parametric Analysis

4.1. Equation Solving. According to Equations (8), (9), and (10), the infinite algebraic equations containing wave field coefficients A_n, B_n, and C_n are expressed as

$$\begin{aligned} \sum_{n=-\infty}^{\infty} A_n \xi_n^{(11)} + \sum_{n=-\infty}^{\infty} B_n \xi_n^{(12)} + \sum_{n=-\infty}^{\infty} C_n \xi_{np}^{(13)} &= \zeta^{(1)}, \\ \sum_{n=-\infty}^{\infty} A_n \xi^{(21)} + \sum_{n=-\infty}^{\infty} B_n \xi_n^{(22)} + \sum_{n=-\infty}^{\infty} C_n \xi_{np}^{(23)} &= \zeta^{(2)}, \\ \sum_{n=-\infty}^{\infty} A_n \xi^{(31)} + \sum_{n=-\infty}^{\infty} B_n \xi_n^{(32)} + \sum_{n=-\infty}^{\infty} C_n \xi_{np}^{(33)} &= \zeta^{(3)}, \end{aligned} \tag{16}$$

where

$$\xi_n^{(11)} = \gamma_{n2} \cdot e^{i\theta_2} - \lambda_{n2} \cdot e^{-i\theta_2}, \xi_n^{(12)} = \varphi_{n2} \cdot e^{i\theta_2} - \psi_{n2} \cdot e^{-i\theta_2}, \xi_{np}^{(13)} = 0,$$

$$\begin{aligned}\xi_n^{(21)} &= H_n{}^{(1)}(k|z|)\left(\frac{z}{|z|}\right)^n + H_n{}^{(1)}(k|z|)\left(\frac{z}{|z|}\right)^{-n} + (-1)^n H_n{}^{(1)}(k|z|)\left(\frac{z}{|z|}\right)^{-n} \\ &\quad \cdot + (-1)^n H_n{}^{(1)}(k|z|)\left(\frac{z}{|z|}\right)^n, \xi_n^{(22)} \\ &= H_n^{(1)}(k|z+d+\mathrm{i}h|)\left(\frac{z+d+\mathrm{i}h}{|z+d+\mathrm{i}h|}\right)^n \\ &\quad + H_n^{(1)}(k|z+d-\mathrm{i}h|)\left(\frac{z+d-\mathrm{i}h}{|z+d-\mathrm{i}h|}\right)^{-n} \\ &\quad + (-1)^n H_n^{(1)}(k|z-d-\mathrm{i}h|)\left(\frac{z-d-\mathrm{i}h}{|z-d-\mathrm{i}h|}\right)^{-n} \\ &\quad + (-1)^n H_n^{(1)}(k|z-d+\mathrm{i}h|)\left(\frac{z-d+\mathrm{i}h}{|z-d+\mathrm{i}h|}\right)^n,\end{aligned}$$

$$\xi_{np}^{(23)} = -J_{np}(k|z+a|)\left(\frac{z+a}{|z+a|}\right)^{np} - J_{np}(k|z+a|)\left(\frac{z+a}{|z+a|}\right)^{-np},$$

$$\xi_n^{(31)} = \gamma_n \cdot e^{i\theta} - \lambda_n \cdot e^{-i\theta}, \xi_n^{(32)} = \varphi_n \cdot e^{i\theta} - \psi_n \cdot e^{-i\theta}, \xi_{np}^{(33)} = \delta_{np} \cdot e^{-i\theta} - \phi_{np} \cdot e^{i\theta},$$

$$\begin{aligned}\zeta^{(1)} &= -\mathrm{i}\cos(\theta_2 - \alpha_0)\exp\left\{\frac{\mathrm{i}k}{2}\left((z_2 - d - \mathrm{i}h)e^{-\mathrm{i}\alpha_0} + \overline{(z_2 - d - \mathrm{i}h)}e^{\mathrm{i}\alpha_0}\right)\right\} - \mathrm{i}\cos(\theta_2 - \gamma_0)\exp \\ &\quad \cdot \left\{\frac{\mathrm{i}k}{2}\left((z_2 - d - \mathrm{i}h)e^{-\mathrm{i}\gamma_0} + \overline{(z_2 - d - \mathrm{i}h)}e^{\mathrm{i}\gamma_0}\right)\right\} \\ &\quad - \mathrm{i}\cos(\theta_2 - \alpha_1)\exp\left\{\frac{\mathrm{i}k}{2}\left((z_2 - d - \mathrm{i}h)e^{-\mathrm{i}\alpha_1} + \overline{(z_2 - d - \mathrm{i}h)}e^{\mathrm{i}\alpha_1}\right)\right\} - \mathrm{i}\cos(\theta_2 - \gamma_1)\exp \\ &\quad \cdot \left\{\frac{\mathrm{i}k}{2}\left((z_2 - d - \mathrm{i}h)e^{-\mathrm{i}\gamma_1} + \overline{(z_2 - d - \mathrm{i}h)}e^{\mathrm{i}\gamma_1}\right)\right\},\end{aligned}$$

$$\zeta^{(2)} = -\exp\frac{ik}{2}\left(ze^{-i\alpha_0} + \bar{z}e^{i\alpha_0}\right) - \exp\frac{ik}{2}\left(ze^{-i\gamma_0} + \bar{z}e^{i\gamma_0}\right) - \exp\frac{ik}{2}\left(ze^{-i\alpha_1} + \bar{z}e^{i\alpha_1}\right) - \exp\frac{ik}{2}\left(ze^{-i\gamma_1} + \bar{z}e^{i\gamma_1}\right),$$

$$\begin{aligned}\zeta^{(3)} &= -\mathrm{i}\cos(\theta - \alpha_0)\exp\left\{\frac{\mathrm{i}k}{2}\left(ze^{-\mathrm{i}\alpha_0} + \bar{z}e^{\mathrm{i}\alpha_0}\right)\right\} - \mathrm{i}\cos(\theta - \gamma_0)\exp\left\{\frac{\mathrm{i}k}{2}\left(ze^{-\mathrm{i}\gamma_0} + \bar{z}e^{\mathrm{i}\gamma_0}\right)\right\} \\ &\quad - \mathrm{i}\cos(\theta - \alpha_1)\exp\left\{\frac{\mathrm{i}k}{2}\left(ze^{-\mathrm{i}\alpha_1} + \bar{z}e^{\mathrm{i}\alpha_1}\right)\right\} - \mathrm{i}\cos(\theta - \gamma_1)\exp\left\{\frac{\mathrm{i}k}{2}\left(ze^{-\mathrm{i}\gamma_1} + \bar{z}e^{\mathrm{i}\gamma_1}\right)\right\},\end{aligned} \tag{17}$$

wherein

$$\begin{aligned}\gamma_{n2} &= H_{n-1}^{(1)}(k|z_2 - d - \mathrm{i}h|)\left(\frac{z_2 - d - \mathrm{i}h}{|z_2 - d - \mathrm{i}h|}\right)^{n-1} - H_{n+1}^{(1)}(k|z_2 - d - \mathrm{i}h|)\left(\frac{z_2 - d - \mathrm{i}h}{|z_2 - d - \mathrm{i}h|}\right)^{-n-1} \\ &\quad - (-1)^n H_{n+1}^{(1)}(k|z_2 - d - \mathrm{i}h|)\left(\frac{z_2 - d - \mathrm{i}h}{|z_2 - d - \mathrm{i}h|}\right)^{-n-1} \\ &\quad + (-1)^n H_{n-1}^{(1)}(k|z_2 - d - \mathrm{i}h|)\left(\frac{z_2 - d - \mathrm{i}h}{|z_2 - d - \mathrm{i}h|}\right)^{n-1},\end{aligned}$$

$$\begin{aligned}\lambda_{n2} &= H_{n+1}^{(1)}(k|z_2 - d - \mathrm{i}h|)\left(\frac{z_2 - d - \mathrm{i}h}{|z_2 - d - \mathrm{i}h|}\right)^{n+1} - H_{n-1}^{(1)}(k|z_2 - d - \mathrm{i}h|)\left(\frac{z_2 - d - \mathrm{i}h}{|z_2 - d - \mathrm{i}h|}\right)^{-n+1} \\ &\quad - (-1)^n H_{n-1}^{(1)}(k|z_2 - d - \mathrm{i}h|)\left(\frac{z_2 - d - \mathrm{i}h}{|z_2 - d - \mathrm{i}h|}\right)^{-n+1} \\ &\quad + (-1)^n H_{n+1}^{(1)}(k|z_2 - d - \mathrm{i}h|)\left(\frac{z_2 - d - \mathrm{i}h}{|z_2 - d - \mathrm{i}h|}\right)^{n+1},\end{aligned}$$

$$\begin{aligned}\varphi_{n2} &= H_{n-1}^{(1)}(k|z_2|)\left(\frac{z_2}{|z_2|}\right)^{n-1} - H_{n+1}^{(1)}(k|z_2 - 2\mathrm{i}h|) \cdot \left(\frac{z_2 - 2\mathrm{i}h}{|z_2 - 2\mathrm{i}h|}\right)^{-n-1} - (-1)^n H_{n+1}^{(1)}(k|z_2 - 2d - 2\mathrm{i}h|) \\ &\quad \cdot \left(\frac{z_2 - 2d - 2\mathrm{i}h}{|z_2 - 2d - 2\mathrm{i}h|}\right)^{-n-1} + (-1)^n H_{n-1}^{(1)}(k|z_2 - 2d|) \cdot \left(\frac{z_2 - 2d}{|z_2 - 2d|}\right)^{n-1},\end{aligned}$$

$$\begin{aligned}\psi_{n2} &= H_{n+1}^{(1)}(k|z_2|)\left(\frac{z_2}{|z_2|}\right)^{n+1} - H_{n-1}^{(1)}(k|z_2 - 2\mathrm{i}h|) \cdot \left(\frac{z_2 - 2\mathrm{i}h}{|z_2 - 2\mathrm{i}h|}\right)^{-n+1} - (-1)^n H_{n-1}^{(1)}(k|z_2 - 2d - 2\mathrm{i}h|) \\ &\quad \cdot \left(\frac{z_2 - 2d - 2\mathrm{i}h}{|z_2 - 2d - 2\mathrm{i}h|}\right)^{-n+1} + (-1)^n H_{n+1}^{(1)}(k|z_2 - 2d|) \cdot \left(\frac{z_2 - 2d}{|z_2 - 2d|}\right)^{n+1},\end{aligned}$$

$$\gamma_n = H_{n-1}^{(1)}(k|z|)\left(\frac{z}{|z|}\right)^{n-1} - H_{n+1}^{(1)}(k|z|)\left(\frac{z}{|z|}\right)^{-n-1} - (-1)^n H_{n+1}^{(1)}(k|z|)\left(\frac{z}{|z|}\right)^{-n-1} + (-1)^n H_{n-1}^{(1)}(k|z|)\left(\frac{z}{|z|}\right)^{n-1},$$

$$\lambda_n = H_{n+1}^{(1)}(k|z|)\left(\frac{z}{|z|}\right)^{n+1} - H_{n-1}^{(1)}(k|z|)\left(\frac{z}{|z|}\right)^{-n+1} - (-1)^n H_{n-1}^{(1)}(k|z|)\left(\frac{z}{|z|}\right)^{-n+1} + (-1)^n H_{n+1}^{(1)}(k|z|)\left(\frac{z}{|z|}\right)^{n+1},$$

$$\varphi_n = H_{n-1}^{(1)}(k|z+d+\mathrm{i}h|)\left(\frac{z+d+\mathrm{i}h}{|z+d+\mathrm{i}h|}\right)^{n-1} - H_{n+1}^{(1)}(k|z+d-\mathrm{i}h|)\left(\frac{z+d-\mathrm{i}h}{|z+d-\mathrm{i}h|}\right)^{-n-1} - (-1)^n H_{n+1}^{(1)}(k|z-d-\mathrm{i}h|)\left(\frac{z-d-\mathrm{i}h}{|z-d-\mathrm{i}h|}\right)^{-n-1} + (-1)^n H_{n-1}^{(1)}(k|z-d+\mathrm{i}h|)\left(\frac{z-d+\mathrm{i}h}{|z-d+\mathrm{i}h|}\right)^{n-1},$$

$$\psi_n = H_{n+1}^{(1)}(k|z+d+\mathrm{i}h|)\left(\frac{z+d+\mathrm{i}h}{|z+d+\mathrm{i}h|}\right)^{n+1} - H_{n-1}^{(1)}(k|z+d-\mathrm{i}h|)\left(\frac{z+d-\mathrm{i}h}{|z+d-\mathrm{i}h|}\right)^{-n+1} - (-1)^n H_{n-1}^{(1)}(k|z-d+\mathrm{i}h|)\left(\frac{z-d+\mathrm{i}h}{|z-d+\mathrm{i}h|}\right)^{-n+1} + (-1)^n H_{n+1}^{(1)}(k|z-d+\mathrm{i}h|)\left(\frac{z-d+\mathrm{i}h}{|z-d+\mathrm{i}h|}\right)^{n+1},$$

$$\delta_{np} = J_{np+1}(k|z+a|)\left(\frac{z+a}{|z+a|}\right)^{np+1} - J_{np-1}(k|z+a|)\left(\frac{z+a}{|z+a|}\right)^{-np+1},$$

$$\phi_{np} = J_{np-1}(k|z+a|)\left(\frac{z+a}{|z+a|}\right)^{np-1} - J_{np+1}(k|z+a|)\left(\frac{z+a}{|z+a|}\right)^{-np-1}. \tag{18}$$

By using the orthogonality of the periodic functions, the system of Equation (16) is expanded by Fourier series. First, both sides of the system are multiplied by $e^{-\mathbf{i}m\theta}$ and then integrated. Thus, the following system of equations is obtained

$$\begin{aligned}
&\sum_{n=-\infty}^{\infty} A_n \xi_{mn}^{(11)} + \sum_{n=-\infty}^{\infty} B_n \xi_{mn}^{(12)} + \sum_{n=-\infty}^{\infty} C_n \xi_{mnp}^{(13)} = \zeta_m^{(1)},\\
&\sum_{n=-\infty}^{\infty} A_n \xi_{mn}^{(21)} + \sum_{n=-\infty}^{\infty} B_n \xi_{mn}^{(22)} + \sum_{n=-\infty}^{\infty} C_n \xi_{mnp}^{(23)} = \zeta_m^{(2)}, \quad (m = 0, \pm 1, \cdots),\\
&\sum_{n=-\infty}^{\infty} A_n \xi_{mn}^{(31)} + \sum_{n=-\infty}^{\infty} B_n \xi_{mn}^{(32)} + \sum_{n=-\infty}^{\infty} C_n \xi_{mnp}^{(33)} = \zeta_m^{(3)},
\end{aligned} \tag{19}$$

where

$$\begin{aligned}
\xi_{mn}^{(11)} &= \frac{1}{2\pi}\int_{-\pi}^{\pi} \xi_n^{(11)} \cdot e^{-\mathbf{i}m\theta} d\theta,\\
\xi_{mn}^{(12)} &= \frac{1}{2\pi}\int_{-\pi}^{\pi} \xi_n^{(12)} \cdot e^{-\mathbf{i}m\theta} d\theta,\\
\xi_{mnp}^{(13)} &= \frac{1}{2\pi}\int_{-\pi}^{\pi} \xi_{np}^{(13)} \cdot e^{-\mathbf{i}m\theta} d\theta,\\
\xi_{mn}^{(21)} &= \frac{1}{2\pi}\int_{-\pi}^{\pi} \xi_n^{(21)} \cdot e^{-\mathbf{i}m\theta} d\theta,\\
\xi_{mn}^{(22)} &= \frac{1}{2\pi}\int_{-\pi}^{\pi} \xi_n^{(22)} \cdot e^{-\mathbf{i}m\theta} d\theta,\\
\xi_{mnp}^{(23)} &= \frac{1}{2\pi}\int_{-\pi}^{\pi} \xi_{np}^{(23)} \cdot e^{-\mathbf{i}m\theta} d\theta,\\
\xi_{mn}^{(31)} &= \frac{1}{2\pi}\int_{-\pi}^{\pi} \xi_n^{(31)} \cdot e^{-\mathbf{i}m\theta} d\theta,\\
\xi_{mn}^{(32)} &= \frac{1}{2\pi}\int_{-\pi}^{\pi} \xi_n^{(32)} \cdot e^{-\mathbf{i}m\theta} d\theta,\\
\xi_{mnp}^{(33)} &= \frac{1}{2\pi}\int_{-\pi}^{\pi} \xi_{np}^{(33)} \cdot e^{-\mathbf{i}m\theta} d\theta,\\
\zeta_m^{(1)} &= \frac{1}{2\pi}\int_{-\pi}^{\pi} \zeta^{(1)} \cdot e^{-\mathbf{i}m\theta} d\theta,\\
\zeta_m^{(2)} &= \frac{1}{2\pi}\int_{-\pi}^{\pi} \zeta^{(2)} \cdot e^{-\mathbf{i}m\theta} d\theta,\\
\zeta_m^{(3)} &= \frac{1}{2\pi}\int_{-\pi}^{\pi} \zeta^{(3)} \cdot e^{-\mathbf{i}m\theta} d\theta.
\end{aligned} \tag{20}$$

In parametric analysis, m and n specify the upper and lower limits of the truncated series, whose values are uncertain and mainly related to the nondimensional frequency. The key to achieving a converged solution is that the value of m should be four times or greater than n. Singular value decomposition is applied to overdetermined equations, and a unique least-norm square solution is obtained. For all the numerical results demonstrated in this paper, $m = 24$ and $n = m/4 - 1$ are selected in consideration of computational efficiency.

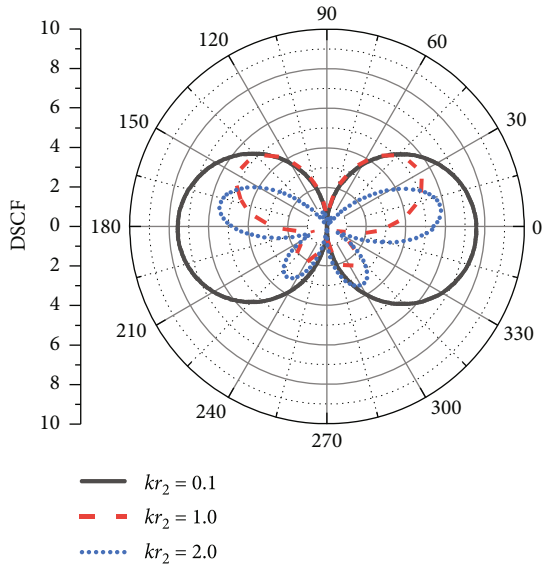

Figure 4: Degradation verification.

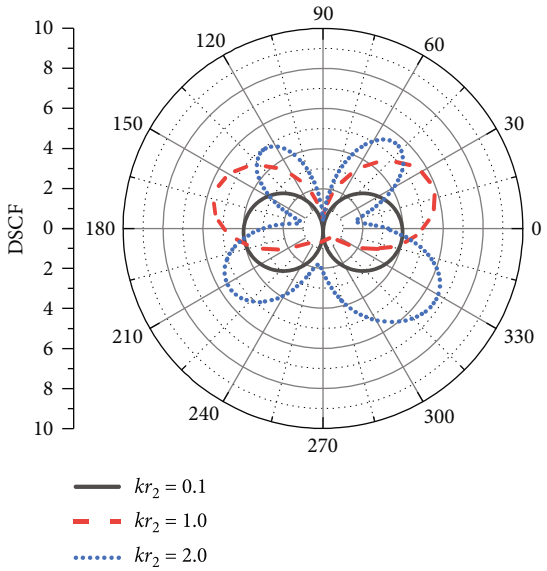

Figure 6: DSCF distribution of the circular hole at different frequencies ($d/r_2 = 3.0$ and $h/r_2 = 5.0$).

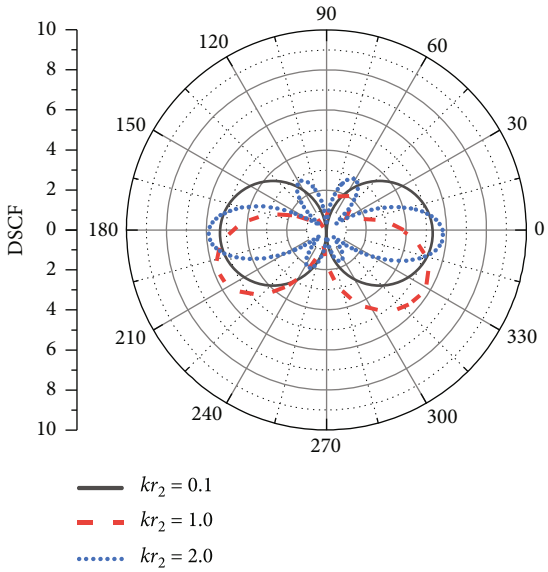

Figure 5: DSCF distribution of the circular hole at different frequencies ($d/r_2 = 8.0$ and $h/r_2 = 7.0$).

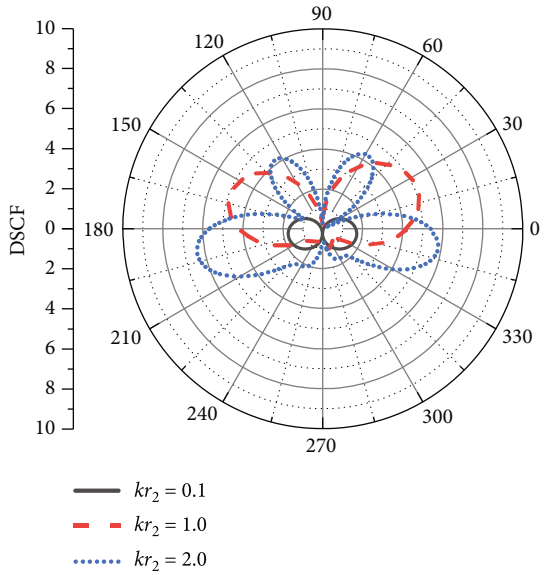

Figure 7: DSCF distribution of the circular hole at different frequencies ($d/r_2 = 5.0$ and $h/r_2 = 2.0$).

4.2. Degradation Verification. The unknown coefficients of each wave field can be obtained by equation solving, and then the DSCF τ_2^* expression can be obtained as follows:

$$\tau_2^* = \left|\tau_{\theta_2 z_2}^{(t)}/\tau_0\right|, \tag{21}$$

where $\tau_{\theta_2 z_2}^{(t)}$ is the total circumferential stress of the circular hole in the coordinate system $(z_2, \overline{z_2})$, and $\tau_0 = \mu k W_0$ is the maximum value of the incident wave stress.

When the position parameters are $h/r_2 = 12.0$, $d/r_2 = 12.0$, and $r_2 = 1.0$, and the shape parameters of the wedge space are $\beta = \pi/2$ and $a = b = r = 0$, then Γ_2 and Γ_3 are collinear. For this case, the SH-wave scattering problem of the wedge-shaped medium with a circular hole is simplified to that of the rectangular-shaped medium. When SH-wave incident vertically at different frequencies, the DSCF distribution of the circular hole is shown in Figure 4. This numerical result is consistent with that reported in reference [11], which proves the correctness of the proposed method.

4.3. Parametric Analysis. Figures 5–7 show the DSCF distribution of the circular hole when the circular hole is in different positions and the SH-wave is incident vertically at

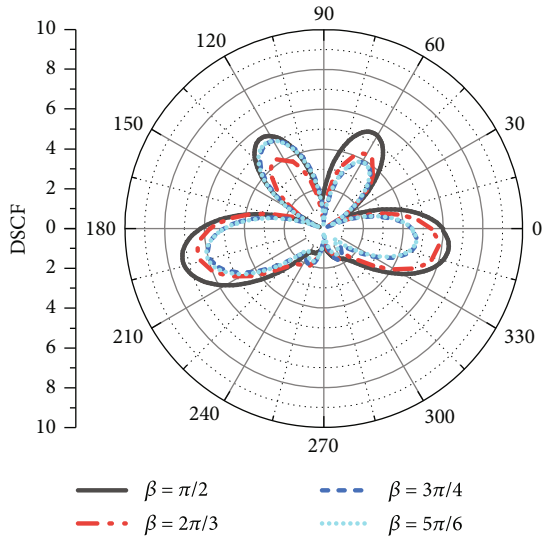

FIGURE 8: DSCF distribution of the circular hole for different values of β ($\alpha_0 = 90\circ$).

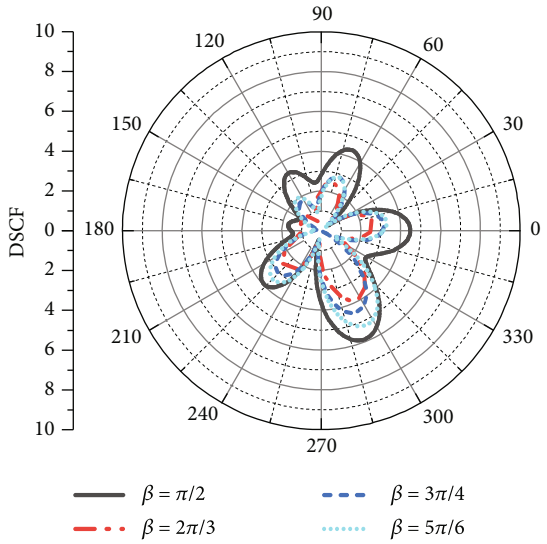

FIGURE 10: DSCF distribution of the circular hole for different values of β ($\alpha_0 = 30\circ$).

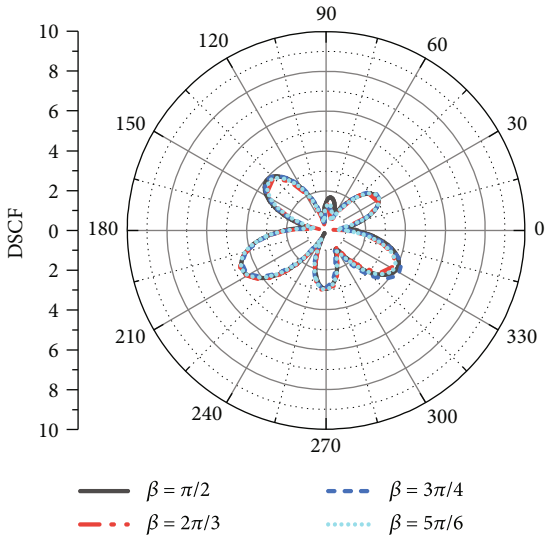

FIGURE 9: DSCF distribution of the circular hole for different values of β ($\alpha_0 = 60\circ$).

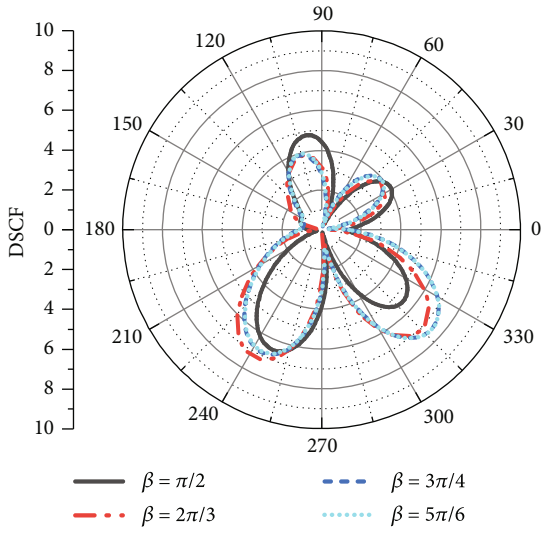

FIGURE 11: DSCF distribution of the circular hole for different values of β ($\alpha_0 = 0\circ$).

different frequencies. The position parameters of the circular hole are randomly selected. The shape parameters of the wedge space are set to $\beta = 2\pi/3$, $b = 1.0$, $a = b/\sqrt{3}$, and $r = r_2 = b = 1.0$. According to Figure 5, when the position parameters of the circular hole are $d/r_2 = 8.0$ and $h/r_2 = 7.0$, the maximum value of the DSCF of the circular hole is 5.27 at low frequency incidence. In medium and high frequency incidence, the maximum value of the DSCF is 5.78 and 5.89, respectively. As can be seen from Figure 6, when the position parameters of the circular hole are $d/r_2 = 3.0$, and $h/r_2 = 5.0$, the maximum value of the DSCF in high frequency incidence is more than that in low and medium frequency incidence. According to Figure 7, when the position parameters of the circular hole are $d/r_2 = 5.0$ and $h/r_2 = 2.0$, the maximum value of the DSCF in medium frequency incidence is about 292.57% of that in low frequency incidence. The maximum value of the DSCF in high frequency incidence is about 365.71% of that in low frequency incidence. Therefore, the DSCF of the circular hole changes dramatically in the medium and high frequency incidence, and the DSCF of the circular hole is the largest at the high frequency incidence, which should be paid special attention to.

Figures 8–11 show the DSCF distribution of the circular hole in the wedge space with different shapes when the SH-wave is incident at different angles at high frequency. The circular hole position parameters are set to $h/r_2 = 5.0$ and $d/r_2 = 2.0$. The wedge shape parameters are set to $\beta = \pi/2$ (right angle case), $\beta = 2\pi/3$, $\beta = 3\pi/4$, $\beta = 5\pi/6$, and $r = r_2$

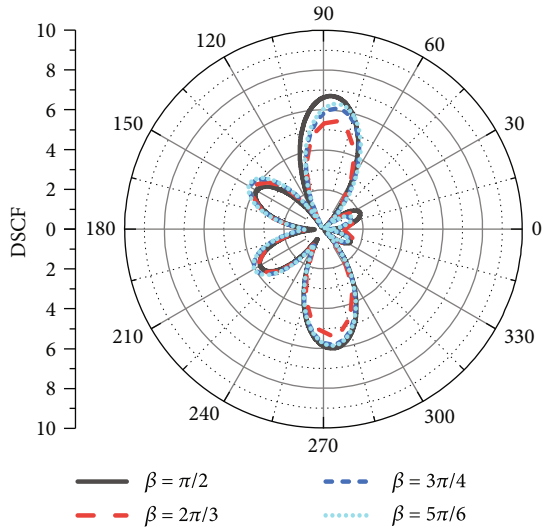

Figure 12: DSCF distribution of the circular hole with different β ($r/r_2 = 0.5$).

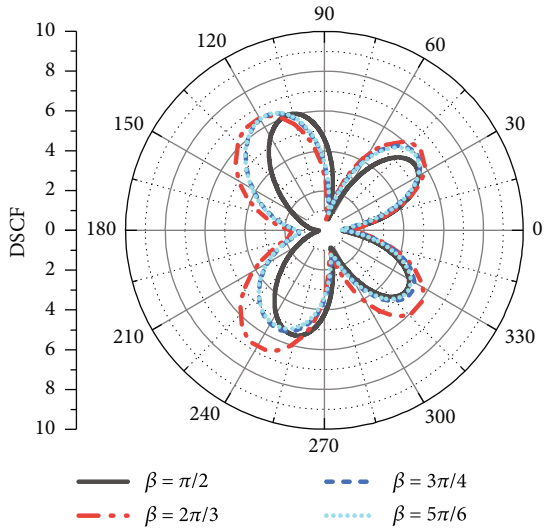

Figure 13: DSCF distribution of the circular hole with different β ($r/r_2 = 1.0$).

$= 1.0$. The values of a and b vary with β. According to Figures 8 and 10, when the SH-wave is incident vertically and at 30°, the appearance of the corner slope has a deamplification effect on the dynamic stress concentration of the circular hole. As can be seen from Figure 9, when the SH-wave is incident at 60°, the change has little influence on the DSCF distribution of the circular hole. According to Figure 11, when the SH-wave is incident horizontally, the maximum value of the DSCF of the circular hole is 6.51 at $\beta = \pi/2$. In the case of $\beta = 2\pi/3$, the maximum value is 7.23, which is about 111.06% of that in the case of $\beta = \pi/2$. In the case of $\beta = 3\pi/4$, the maximum value is 7.44, which is about 114.29% of that in the case of $\beta = \pi/2$. In the case of $\beta = 5\pi/6$, the maximum

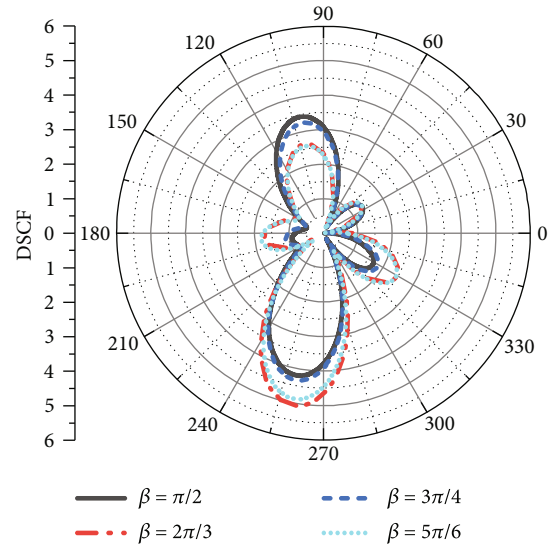

Figure 14: DSCF distribution of the circular hole for different values of β ($r/r_2 = 2.0$).

value is 7.47, which is about 114.75% of that in the case of $\beta = \pi/2$. It can be seen that when the SH-wave is incident horizontally at a high frequency, the appearance of the corner slope will have an amplified effect on the dynamic stress concentration of the circular hole.

Considering that the shape and size of the wedge space are randomly selected in actual engineering, Figures 12–14 show the influences of different shape and size of the wedge space on the dynamic stress concentration of the circular hole under the condition of high frequency incidence of SH-wave at horizontal angle. The circular hole position parameters are set to $h/r_2 = 5.0$ and $d/r_2 = 3.0$. The wedge shape parameters are set to $\beta = \pi/2$, $\beta = 2\pi/3$, $\beta = 3\pi/4$, $\beta = 5\pi/6$, and $r = r_2 = 1.0$. The values of a and b vary with β. r/r_2 represents the size of the circular hole, $r_2 = 1.0$. As can be seen from Figure 12, when $r/r_2 = 0.5$, the change of β has little influence on the DSCF of the circular hole. According to Figure 13, when $r/r_2 = 1.0$, the maximum DSCF value in $\beta = 2\pi/3$ is 6.74, which is about 122.99% of the maximum DSCF value at $\beta = \pi/2$. According to Figure 14, when $r/r_2 = 2.0$, the DSCF value at $\beta = 2\pi/3$ is the largest, which is 120.74% of the maximum DSCF value at $\beta = \pi/2$. It can be concluded that when the corner slope is larger, the change of β has a significant effect on the dynamic stress concentration of the circular hole.

5. Prediction Model

The BP neural network is a multilayer feedback artificial neural network with error back propagation. The hidden layer of the BP neural network model in this paper has 3 layers, and the number of neurons in the hidden layer is 10, 20, and 30, respectively. There are 5 inputs, which are the SH-wave incident parameter, circular hole location parameter, angle parameter of the circular hole boundary, the wedge shape parameter, and size parameter of the wedge

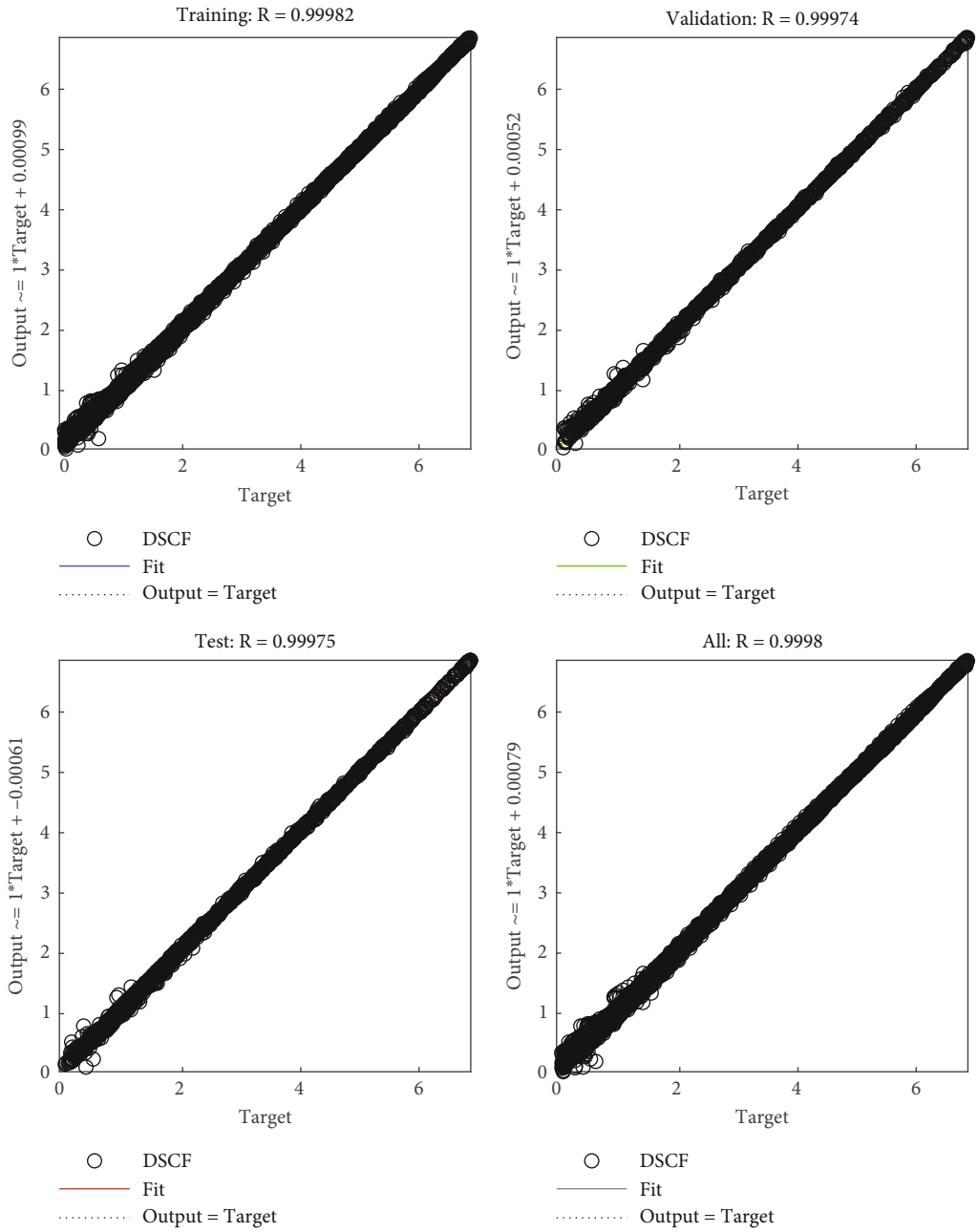

Figure 15: Regression coefficients.

space, respectively. The output is the DSCF of the circular hole. The DSCF is calculated under different conditions, and the data is divided into training sets, verification sets, and test sets. The performance is evaluated according to the training results. The performance of the model is evaluated according to the training results, and the evaluation index is the regression coefficient (R) [26]. The specific expression for the regression coefficient is as follows:

$$R = \sqrt{1 - \frac{\sum_{i=1}^{N}(y_i - f_i)^2}{\sum_{i=1}^{N}(y_i - \bar{y})^2}}, \tag{22}$$

where y_i is the regression observation data, f_i is the regression fitting data, and $\bar{y}$ is the mean value of the observation data. N is the number of samples, and i ranges from $1 \sim N$.

The BP neural network is used to learn and train the data sets of the DSCF, and the obtained R results are shown in Figure 15. The R values of the training set, verification sets, and test sets all reached above 0.99. Figure 16 shows the comparison between the predicted results and the actual results at $\beta = 2\pi/3$ and $r/r_2 = 1.0$ at the high frequency incidence of SH-wave and at the horizontal angle. The predicted results are in good agreement with the actual results. Therefore, the BP neural network has a good prediction

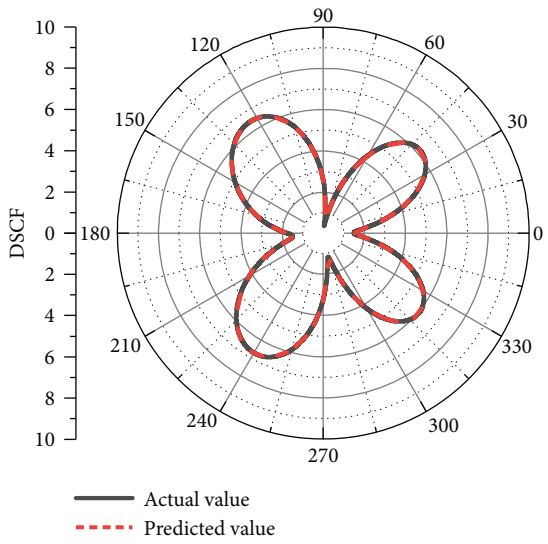

Figure 16: Comparison between actual results and predicted results.

performance in estimating the DSCF of the circular hole in the wedge space.

6. Conclusion

Considering the common application of wedge structures in the field of engineering, the dynamic antiplane characteristics of a circular hole in a wedge-shaped quarter-space are studied based on the wave function expansion method. An analytical solution for the DSCF of the circular hole is obtained. Through the parametric analysis and prediction results, the following conclusions can be drawn:

(1) The dynamic stress concentration of the circular hole in the wedge space is more obvious in the case of high frequency SH-wave compared to medium and low frequency SH-wave

(2) When the SH-wave is in vertical incidence with high frequency and 30° incidence, the corner point slope will have a deamplification effect on the dynamic stress concentration of the circular hole. On the contrary, the horizontal incidence of the SH-wave amplifies the dynamic stress concentration of the circular hole. Among the case considered, the maximum value of DSCF at $\beta = 5\pi/6$ is 7.47, which is about 114.75% of that at $\beta = \pi/2$

(3) When $r/r_2 = 0.5$, the shape parameters of the wedge space have little influence on the dynamic stress concentration of the circular hole. When $r/r_2 = 1.0$ or $r/r_2 = 2.0$, the change of wedge shape parameters has a great influence on the dynamic stress concentration of the circular hole, and in both cases, the maximum DSCF at $\beta = 2\pi/3$ is about 1.2 times the maximum DSCF at $\beta = \pi/2$

(4) Based on the BP neural network, the R value of the DSCF prediction model of the circular hole in the wedge space can reach more than 0.99, and the predicted results are in good agreement with the actual results

The theoretical methods used in this paper can provide a basis for the wedge combination and other related problems. The conclusion and the prediction model can be a reference for the nondestructive testing and fatigue life prediction of the structure and provide a research idea for the inverse problem of the dynamic response in the wedge space.

Data Availability

The data used to support the findings of this study are included within the article.

Conflicts of Interest

The authors declare that there are no conflicts of interest regarding the publication of this paper.

Acknowledgments

This work was supported by the National Natural Science Foundation of China (No. 12002198) and Shanghai "Chenguang" Program (No. 20CG69).

References

[1] S. A. Kumar, R. Rajesh, and S. Pugazhendhi, "A review of stress concentration studies on fibre composite panels with holes/cutouts," *Proceedings of the Institution of Mechanical Engineers, Part L: Journal of Materials: Design and Applications*, vol. 234, no. 11, pp. 1461–1472, 2020.

[2] A. R. Torabi, H. Talebi, M. R. Ayatollahi, and M. Petru, "Mixed mode I-III fracture resistance of stainless steel 316L weakened by V-notches with end holes," *Theoretical and Applied Fracture Mechanics*, vol. 122, article 103574, 2022.

[3] G. Mieczkowski, "Stress fields and fracture prediction for an adhesively bonded bimaterial structure with a sharp notch located on the interface," *Mechanics of Composite Materials*, vol. 53, no. 3, pp. 305–320, 2017.

[4] G. Mieczkowski, "Determination of stress intensity factors for elements with sharp corner located on the interface of a bimaterial structure or homogeneous material," *Acta Mechanica*, vol. 232, no. 2, pp. 709–724, 2021.

[5] V. W. Lee and R. I. Sherif, "Diffraction around circular canyon in elastic wedge space by plane SH-waves," *Journal of Engineering Mechanics-Proceedings of the ASCE*, vol. 122, no. 6, pp. 539–544, 1996.

[6] N. Dermendjian and V. W. Lee, "Moment solution of antiplane (SH) wave diffraction around arbitrary-shaped rigid foundations on a wadge-shape half space," *ISET Journal of Earthquake Technology*, vol. 40, no. 4, pp. 161–172, 2003.

[7] N. Dermendjian, V. W. Lee, and J. W. Liang, "Anti-plane deformations around arbitrary-shaped canyons on a wedge-shape half-space: moment method solutions," *Earthquake Engineering and Engineering Vibration*, vol. 2, no. 2, pp. 281–287, 2003.

[8] Q. J. Liu, Z. Y. Wu, and V. W. Lee, "Scattering and reflection of SH waves around a slope on an elastic wedged space," *Earthquake Engineering and Engineering Vibration*, vol. 18, no. 2, pp. 255–266, 2019.

[9] W. P. Shi, J. L. Chu, and L. C. Li, "Scattering of steady incident sh-wave by circular arc lining at the corner point of rectangular plane," *Mechanics in Engineering*, vol. 28, no. 5, pp. 34–38, 2006.

[10] W. P. Shi, D. K. Liu, Y. T. Song, J. L. Chu, and A. Q. Hu, "Scattering of circular cavity in right-angle planar space to steady SH-wave," *Applied Mathematics and Mechanics*, vol. 27, no. 12, pp. 1619–1626, 2006.

[11] Y. Shi, H. Qi, and Z. L. Yang, "Scattering of SH-wave by circular cavity in right-angle plane and seismic ground motion," *Chinese Journal of Applied Mechanics*, vol. 25, no. 3, pp. 392–397, 2008.

[12] D. H. Tsaur and K. H. Chang, "Exact solution to scattering of SH waves by an elliptic-arc canyon in the corner of an elastic quarter space," *Soil Dynamics and Earthquake Engineering*, vol. 110, no. 1, pp. 137–140, 2018.

[13] G. Liu, B. H. Ji, H. T. Chen, and D. Liu, "Antiplane harmonic elastodynamic stress analysis of an infinite wedge with a circular cavity," *Journal of Applied Mechanics*, vol. 76, no. 6, article 061008, 2009.

[14] Z. X. Liu and J. W. Liang, "Analytic diffraction solution of plane SH waves by a circular canyon in wedge-shaped space," *Chinese Quarterly of Mechanics*, vol. 31, no. 3, pp. 363–370, 2010.

[15] Z. X. Liu and J. W. Liang, "Analytic solution for diffraction of plane SH waves by a circular alluvial valley in wedge-shaped space," *Journal of Tianjin University*, vol. 43, no. 7, pp. 573–582, 2010.

[16] H. F. Kara, "Diffraction of plane SH Waves by a cylindrical cavity in an infinite wedge," *Procedia engineering*, vol. 161, pp. 1601–1607, 2016.

[17] H. F. Kara, "A note on response of tunnels to incident SH-waves near hillsides," *Soil Dynamics and Earthquake Engineering*, vol. 90, pp. 138–146, 2016.

[18] Z. L. Yang, X. Z. Li, Y. Q. Song, G. Jiang, M. Sun, and X. Fang, "Scattering of SH waves around circular canyon in inhomogeneous wedge space," *Geophysical Journal International*, vol. 223, no. 1, pp. 45–56, 2020.

[19] Z. L. Yang, X. Z. Li, Y. Q. Song, G. Jiang, M. Sun, and X. Fang, "Erratum: 'scattering of SH waves around circular canyon in inhomogeneous wedge space'," *Geophysical Journal International*, vol. 226, no. 1, pp. 345–350, 2021.

[20] M. Treifi and S. O. Oyadiji, "Evaluation of mode III stress intensity factors for bi-material notched bodies using the fractal-like finite element method," *Computers & Structures*, vol. 129, pp. 99–110, 2013.

[21] C. Cheng, Z. Niu, and N. Recho, "Analysis of the stress singularity for a bi-material V-notch by the boundary element method," *Applied Mathematical Modelling*, vol. 37, no. 22, pp. 9398–9408, 2013.

[22] X. C. Ping, L. Leng, and S. H. Wu, "Thermo-mechanical stress near apex of a bi-material wedge by a novel finite element analysis," *Key Engineering Materials*, vol. 525-526, pp. 9396–9526, 2013.

[23] Z. X. Liu and L. Liu, "An IBEM solution to the scattering of plane SH-waves by a lined tunnel in elastic wedge space," *Earthquake Science*, vol. 28, no. 1, pp. 71–86, 2015.

[24] Z. X. Liu, L. Liu, and J. W. Liang, "Solving the scattering of plane SH-waves by an arbitrary shaped cavity embedded in a wedge-shaped space by IBEM," *Acta Mechanica Solida Sinica*, vol. 35, no. 3, pp. 292–301, 2014.

[25] G. Mieczkowski, D. Szpica, A. Borawski, M. M. Awad, A. Elgarayhi, and M. Sallah, "Investigation of the near-tip stress field of a notch terminating at a bi-material Interface," *Materials*, vol. 14, no. 16, p. 4466, 2021.

[26] H. F. Lu, X. Ma, M. D. Ma, and S. Zhu, "Energy price prediction using data-driven models: a decade review," *Computer Science Review*, vol. 39, article 100356, 2021.

[27] F. Sen, K. M. Aydin, and O. Sayman, "Prediction of bearing strength of two serial pinned/bolted composite joints using artificial neural networks," *Journal of Composite Materials*, vol. 44, no. 11, pp. 1365–1377, 2010.

[28] S. Lari, Y. J. Qian, and H. J. Kwon, "Assessment of geometrical features of internal flaws with artificial neural network," *International Journal of Precision Engineering and Manufacturing*, vol. 22, no. 5, pp. 777–789, 2021.

[29] H. Qi and X. M. Zhang, "Scattering of SH-wave by a circular inclusion near the interfacial cracks in the piezoelectric bimaterial half-space," *Journal of Mechanics*, vol. 34, no. 3, pp. 337–347, 2018.

[30] Z. L. Yang, C. Q. Zhang, Y. Yang et al., "Scattering of out-plane wave by a circular cavity near the right-angle interface in the exponentially inhomogeneous media," *Wave Motion*, vol. 72, pp. 354–362, 2017.

[31] Y. F. Gao and N. Zhang, "Scattering of cylindrical SH waves induced by a symmetrical V-shaped canyon: near-source topographic effects," *Geophysical Journal International*, vol. 193, no. 2, pp. 874–885, 2013.

[32] D. H. Tsaur, K. H. Chang, and M. S. Hsu, "An analytical approach for the scattering of SH waves by a symmetrical V-shaped canyon: deep case," *Geophysical Journal International*, vol. 183, no. 3, pp. 1501–1511, 2010.